Mechanical manipulation of graphene nanoribbons on Au(111) using large amplitude scanning force microscopy experiments and calculations

Sebastian Schneider,[1] Jonathan Eifler,[2] Olga Artemyeva,[3] Tillmann Klamroth,[2] and Regina Hoffmann-Vogel[3,*]

[1]*Physikalisches Institut, Karlsruhe Institute of Technology, Wolfgang-Gaede-Strasse 1, D-76128 Karlsruhe, Germany*

[2]*Institute of Chemistry, University of Potsdam, Karl-Liebknecht-Strasse 24-25, 14476 Potsdam-Golm, Germany*

[3]*Institute of Physics and Astronomy, University of Potsdam, Karl-Liebknecht-Strasse 24-25, 14476 Potsdam-Golm, Germany*

(Received 10 November 2025; accepted 27 March 2026; published 22 April 2026)

We investigate the manipulation of weakly bound graphene nanoribbons (GNRs) on the Au(111) surface using large amplitude scanning force microscopy. The GNRs are fabricated *in situ* via surface-assisted Ullmann coupling. Mobile GNRs are identified in scanning images by increased noise due to their weak binding. Their mobility is reduced when they are part of an extended GNR network. Even during passive imaging, interactions between the tip and the GNR can induce slight movements, allowing us to approximate the corrugation of the surface binding potential. We demonstrate tip-induced rotation and lateral displacement of GNRs perpendicular to their axis, during which the ribbon is partially lifted from the surface. Based on first-principles calculations, we construct a two-dimensional potential energy landscape and perform climbing image nudged elastic band calculations to approximate energy barriers for translation. Both approaches show that the barrier strongly depends on the GNR orientation. In addition, we find that beyond a critical length, GNRs become effectively immobilized due to increased energy barriers and reduced flexibility. The theoretical results align well with the observed outcomes of the manipulation experiments.

DOI: 10.1103/5t5n-p5pl

I. INTRODUCTION

Single atoms, CO, molecular islands and nanocrystals have been manipulated mechanically by scanning tunneling microscopy using electromigration forces [1–4]. Manipulating atoms or molecules with scanning force microscopy (SFM) has followed [5]. If SFM is used for mechanical manipulation, then the force needed to move the object can be measured [6] and the binding energy of a molecule to the surface can be determined [7]. However, there is an additional complication compared to scanning tunneling microscopy, because in the main measurement mode (dynamic mode) used for atomic resolution [8,9] the tip is oscillated and may not remain in permanent contact with the object to be manipulated. Therefore, in most manipulation studies, quartz crystal tuning forks and oscillation amplitudes below 0.1 nm are used [6,10]. In addition bimodal oscillation of cantilevers also with small oscillation amplitudes (0.3 nm) was used successfully for manipulation [11]. For such manipulation experiments, lowering the diffusion barrier by the presence of the tip was discussed as a possible manipulation mechanism [12,13]. Using large oscillation amplitudes (2 to 66 nm) the manipulation of single atoms and defects on insulators or semiconductors at room temperature has also been demonstrated [5,14,15]. For large amplitude manipulation experiments, mechanisms of manipulation are discussed additionally involving vertical manipulation and/or long jumps of the object to be manipulated [5,16].

Graphene nanoribbons (GNRs) have attracted interest due to their peculiar electronic properties, e.g., due to the confinement of electrons in the ribbons and the possibility of engineering the energy gap by influencing the width of the ribbons [17,18]. In particular GNRs terminated with armchair edges are semiconducting whereas GNRs terminated by zigzag edges are metallic (gapless). The local work function has been studied [19] and electrostatic effects at the nanoribbon edges [20]. Electronic properties such as the conductance have been studied by manipulation-related techniques, such as lifting [21]. Perfecting molecular manipulation could help to position a molecule, e.g., a graphene nanoribbon, between two metallic contacts for molecular electronics experiments in vacuum, where they are more independent of possible contamination. The force needed for manipulation of a graphene nanoribbon along its length has been measured using small oscillation amplitudes (40 pm) [10]. Superlubricity has been found where friction nearly vanishes.

GNRs have also received considerable theoretical interest. In 2011 Björk *et al.* [22] proposed a mechanism for the formation of GNRs from polyanthracene via a cyclodehydrogenation step. Later, another mechanism was discussed in a paper by Blankenburg *et al.* [23], which was also assumed with the STM induced formation of heterojunction. Other studies further explored the STM-induced reaction by using quasi-freestanding polyanthrylene chains [24,25]. Later,

*Contact author: hoffmannvogel@uni-potsdam.de

Ma *et al.* [26] critically reexamined the previously proposed mechanisms and, based on deuterium-labeling experiments, concluded that both earlier pathways were incorrect. They proposed an alternative mechanism that better explains the observed reaction behavior. Theoretical studies have explored the manipulation of GNRs on Au(111) using force fields such as the Embedded Atom Method (EAM) [27] and the reactive empirical bond order (REBO) potential [28]. In these simulations, the GNR is moved laterally over the surface from one end, accompanied by partial detachment and bending.

Here, we show the manipulation of single GNRs on the Au(111) surface using dynamic mode cantilever-scanning force microscopy with large oscillation amplitudes. The substrate is cooled by liquid nitrogen. The tips are not cooled in our set-up and remain near room temperature. Weakly bound GNRs on the surface can be manipulated easily, i.e., rotated or displaced in the direction perpendicular to their length. When the graphen nanoribbon binds to a network structure, the nanoribbon is stable against manipulation. Weakly bound nanoribbons are detected through their noisy appearance. An influence of the tip's scanning motion on the nanoribbon position is detected and used to estimate the surface binding potential corrugation. During manipulation the nanoribbon is partly lifted from the surface. Our first-principles calculations have allowed us to construct a two-dimensional potential energy landscape for GNRs. On this basis we have performed climbing image nudged elastic band (CI-NEB) calculations to approximate energy barriers for translation. In both descriptions, the energy barrier strongly depends on the GNR orientation similar to the experimental observation. Beyond a critical length, GNRs become effectively immobilized due to increased energy barriers and reduced flexibility.

II. METHODS

We prepare GNRs *in situ* by surface-assisted Ullmann-coupling using 10,10'-Dibromo-9,9'-bianthryl (DBBA) precursor molecules on the Au(111) surface [29]. We use commercially available Au(111) on Mica substrates (Phasis, Plan-les-Oates, Switzerland). We mount them in thermal contact to a Ta stripe for direct current heating. We clean the Au(111) surface by sputtering and annealing cycles using Ar ion sputtering. We have carefully checked the self-assembly of the precursor molecules at room temperature [30]. We check the substrate cleanliness by scanning force microscopy imaging in the same vacuum system having a base pressure on the order of 10^{-9} Pa. After that we deposit DBBA on the preheated (180 °C) substrate by thermal evaporation. GNRs are obtained after annealing to 250 °C for 2 h and subsequently to 420 °C for 1 h.

Scanning force microscopy imaging and manipulation is performed in our variable temperature scanning force microscope from Omicron (VT-AFM-XA, Omicron, Taunusstein, Germany). We use a Nanonis phase-locked loop system (Specs, Switzerland) for controlling the tip oscillation, scanning and manipulation. We image in the dynamic mode, where the tip is oscillated at resonance using a constant oscillation amplitude controlled by a feed-back loop. We measure the frequency using a phase-looked loop system acting on the excitation amplitude. When the tip approaches the surface, the resonance shifts due to the interaction with the sample. This change in resonance is kept constant for topographic imaging using another feed-back loop acting on the tip-sample distance.

For scanning force microscopy manipulation first a path for the horizontal motion of the tip is defined in the SFM controller software. The nanoribbon to be manipulated is intended to be located in the center of this path. We then scan this path several times with a predefined velocity, while lowering the frequency shift between tip and sample by a predefined step before each scan. During the motion of the tip, the z position, the oscillation amplitude and the frequency shift of the tip are observed. A clear change of one of these measured quantities points to an irreversible change of the position of the GNR. With every step of lower frequency shift the interaction between tip and GNR becomes larger. At some point the interaction is so large that the GNR changes position on the substrate. After each scan the tip is brought to the original frequency shift and an overview image is measured to pinpoint possible changes concerning the tip and/or the sample.

All calculations were performed using VASP in the version VASP-5.4.4 [31,32]. We use a projector-augmented plane-wave basis [33,34] with the PBE [35] functional and include dispersion forces via the Grimme D3 method [36] with Becke-Jonson damping [37]. Based on the calculations reported in Ref. [38], we use a cutoff energy of 400 eV. Further, we used 3 layer slabs, which gave reasonably converged results regarding the adsorption energies for the adsorption geometry reported in Ref. [38]. Three layers were also found to be sufficient for the calculation of local work functions in Ref. [19]. The used k-point grids and further details of the calculations can be found in the Appendixes A–F.

III. EXPERIMENTAL RESULTS

Figure 1(a) shows an overview image of graphene nanoribbons with a nominal coverage of 0.7 molecular layers on the Au(111) surface. We observe points where several nanoribbons connect ("knots") and a relatively homogeneous length distribution. A typical knot is marked in blue in Fig. 1(a). In addition, we observe a preferential orientation of the nanoribbons along one of the sixfold substrate symmetry directions, similar to the one observed, e.g., in Refs. [39,40]. By the knots and branches the graphene nanoribbon network is stabilized. These connected nanoribbons are not suitable for manipulation due to their stability.

In addition to these network-stabilized graphene nanoribbons, we find weakly bound graphene nanoribbons, marked by bright ovals. In comparison to the stable network of nanoribbons these appear noisy because they are moved laterally during scanning by the interaction with the tip. To manipulate a graphene nanoribbon, first, a nanoribbon with noisy contrast is identified. The tip is then brought to a position suitable for manipulation, marked in yellow in Fig. 1(b). Then the frequency shift set-point is lowered and the tip is moved along the blue arrow. It is checked whether there is a jump of measured quantities during manipulation. After that the frequency shift set-point is set to its original value and an overview image is taken Figs. 1(c)–1(e). The tip is again moved to the yellow position and the process is repeated with

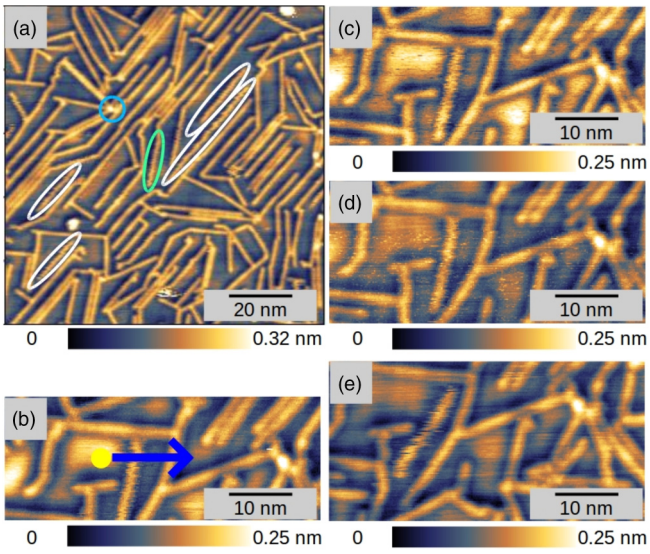

FIG. 1. Manipulation by stepwise approaching and then moving the tip, forward scan images, (a) GNRs are bound with different strength to the substrate. Weakly bound ribbons not connected to a network are marked by white ovals. A point where GNRs are connected is marked with a blue circle. A nanoribbon showing reduced noise is marked by a green oval: $\Delta f = -13$ Hz. (b) The nanoribbon to be manipulated appears noisy due to its mobility and is weakly bound to the substrate. The starting point of the manipulation is marked in yellow and the arrow shows the manipulation path of the tip: $\Delta f = -16$ Hz. (c) Graphene nanoribbon after manipulation at $\Delta f = -50$ Hz. Frequency shift used for imaging: $\Delta f = -16$ Hz. (d) Graphene nanoribbon after manipulation at $\Delta f = -55$ Hz. Frequency shift used for imaging: $\Delta f = -16$ Hz. (e) Graphene nanoribbon after manipulation at $\Delta f = -60$ Hz. The graphene nanoribbon has rotated. For all images $c_L = 37$ N/m, $f_0 = 331$ Hz, $A = 6$ nm, and $Q = 24\,000$.

a lower frequency shift set-point until an irreversible change in position of the nanoribbon is observed. The velocity used for manipulation was 49 nm/s, i.e., one manipulation run was performed in approximately 1 s.

Figures 1(d) and 1(e) show the image of the graphene nanoribbon after attempted manipulation at $\Delta f = -55$ Hz and $\Delta f = -60$ Hz. While in Fig. 1(d) the nanoribbon remains in its original position, in Fig. 1(e) it has rotated by about 24° around a point close to its center near the end of another nanoribbon. Finally, we tried to reverse the rotation by manipulation. This attempt was unsuccessful presumably because the tip did not reach into the space between the nanoribbon to be rotated and its neighboring nanoribbon on the right hand side. Another possibility is that it the nanoribbon to be rotated is now bound too strongly to neighboring nanoribbons. This possibility is supported by the observation of an additional kink introduced to the nanoribbon near its end at the lower left side. Here, the two nanoribbons are located parallel to each other and this configuration could enhance a larger mutual binding energy of the two ribbons. Another possibility, as detailed in the DFT section below, is that the rotation results from a reorientation of the GNR on the surface. A reverse rotation is energetically unfavorable and therefore does not occur.

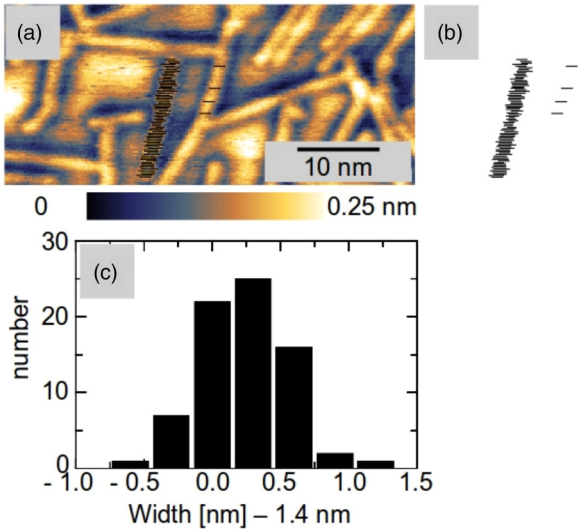

FIG. 2. (a) Same image as Fig. 1(c) where lines representing the noisy graphene nanoribbon were added to each scanline. In addition the width of a bound graphene nanoribbon that does not appear noisy was measured by four additional lines and determined to be 1.4 nm. (b) Added lines are shown for clarity without the measured image. (c) From the width of these added lines a histogram of the apparent width of the noisy graphene nanoribbon was generated. In most scanlines the noisy graphene nanoribbon appears wider than the bound ribbon of width 1.4 nm. The bin size of the histogram was chosen to be 0.3 nm because this is the approximate atomic distance on the Au(111) herringbone reconstruction in the direction perpendicular to the herringbone lines.

To find out more details about the noise and the potential energy landscape we have analyzed in detail the noise observed on the nanoribbon in Fig. 1(c), see Fig. 2. For the different scanlines, both the width and the lateral position of the nanoribbon vary at the atomic scale. A varying width of the nanoribbon could be a sign for a hop of its position while it interacts with the tip during scanning: If the nanoribbon appears wider than expected, then this could be explained by a hop in the scan direction. If the nanoribbon appears narrower than expected, then this could be explained by a hop against the scan direction. A varying position is related to the sum of the jumps the nanoribbon carries out during one full scan cycle including forward and backward scan. We have analyzed the width of the nanoribbon for 74 scanlines.

We compare the nanoribbon width with a typical width of a nanoribbon oriented in the same direction as the one to be investigated; see Fig. 2(a). Also the apparent width of this strongly bound nanoribbon shows small variations along its length, partly because the apparent height of the Au background varies locally. These variations are clearly distinct from the appearance of the loosely bound nanoribbon. We determine the average width of the strongly bound nanoribbon to be 1.4 nm in the direction of the scan. Compared to this average width, the loosely bound nanoribbon appears 22 times similar, 44 times wider, and 8 times narrower, indicating that nanoribbon hops in the direction of the scan are much more probable compared to the opposite direction. A histogram of the loosely bound nanoribbon's apparent width is shown in

TABLE I. List of the binding energies, E_B, the barriers, $\Delta V_{\text{Pot.}}$, of the interpolated potential [cf. Fig. 6(b)] along the direction perpendicular to the GNR, the energy barrier of the CI-NEB-calculation $\Delta V_{\text{CI-NEB}}$, the second derivative of these potentials at the minimum, $k_{\text{prep.}}$, and the corresponding harmonic frequency for the frustrated GNR translation. E_B, ΔV, and $k_{\text{prep.}}$ are normalized with respect to n_{GNR}.

Ads. direction	A	B	C	D
$\Delta V_{\text{Pot.}}$ [eV]	0.072	0.027	0.011	0.006
$\Delta V_{\text{CI-NEB}}$ [eV]	0.050	0.015	0.002	0.002
$k_{\text{prep.}}$ [eV/Å^2]	0.246	0.099	0.071	0.031
ν_{harm} [1/s]	5.9×10^{11}	3.7×10^{11}	3.2×10^{11}	2.1×10^{11}

Fig. 2(c). The bin size of the histogram was chosen to be 0.3 nm since the interatomic distance on the Au(111) surface has this value. The histogram shows that most probably the nanoribbon hops one atomic step forward during the interaction time with the tip, but also no hop, backward hops, and multiple forward hops are observed with less probability.

A similar analysis for the backward scan direction showed no broadening of the graphene nanoribbon. Presumably the nanoribbon can move more easily in the direction pointing away from the neighboring nanoribbon than in the opposite direction. The overview image of Fig. 1(a) shows that noise for several nanoribbons depends on their orientation with respect to the substrate. For example, the nanoribbon marked with a green oval shows less noise compared to the nanoribbons marked with white ovals.

These hops can be explained by the mechanisms discussed in literature: the energy barrier between two neighboring states could be lowered due to the interaction with the tip [12,13], or the temperature of the nanoribbon could increase due to the presence of the tip [41]. Since the tip remains near room temperature in this experiment while the nanoribbon is cooled, it is likely that the temperature of the nanoribbon is raised by the presence of the tip. This change in temperature would however not lead to an asymmetry in the forward and backward hopping. The asymmetry could be related to a lowering of the energy barrier relevant for hopping due to the presence of the tip. Assuming one hop per scan and a thermal activation hopping rate of $\gamma = \gamma_0 \exp(-\Delta E/k_B T) = 1/\text{s}$ with $\gamma_0 = 10^{12}$ Hz and T between 115 K and room temperature gives $\Delta E = 270$–710 meV. We set the value of γ_0 slightly higher than the estimated vibrational frequency for the lateral motion of the whole rigid GNR derived from our two-dimensional (2D) potential (see below and Table I), because preexponential factors for surface reactions are often dominated by entropic effects and thus can be larger than the actual vibrational frequencies (see, for instance, Ref. [42]). Furthermore, we note that γ_0 enters only logarithmically in the calculation of ΔE.

An analysis of noise had been done before for truxenes on a KBr(001) surface [43]. Truxenes are bound much more loosely to a KBr(001) step compared to nanoribbons on Au. In that study the width of the truxene image was related to the residence time of the molecule near the step. Configurational entropy detected through molecular hops was analyzed in detail previously [44].

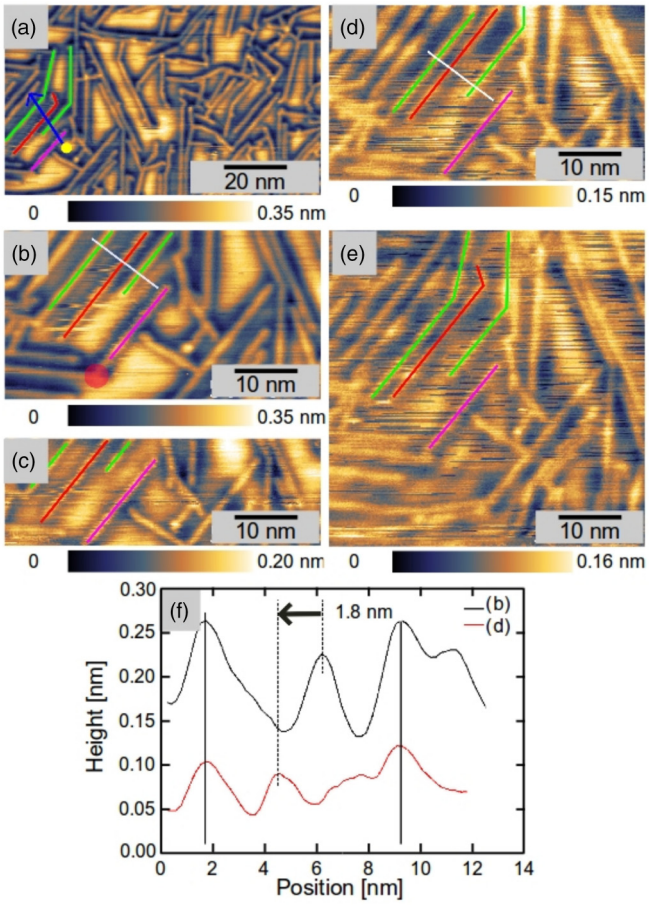

FIG. 3. Manipulation of graphene nanoribbons bound to the substrate with different strength. (a) The nanoribbons to be manipulated are marked in red and purple. The starting point of the manipulation path is marked in yellow and the manipulation path is marked by a blue arrow. $\Delta f = -15$ Hz. (b) The purple graphene nanoribbon is bound to another nanoribbon at the point marked by a red circle ($\Delta f = -15$ Hz). (c) Graphene nanoribbons after attempted manipulation at $\Delta f = -60$ Hz. Frequency shift used for imaging $\Delta f = -15$ Hz. (d) Graphene nanoribbons after attempted manipulation at $\Delta f = -75$ Hz. The red graphene nanoribbon has changed position. Frequency shift used for imaging $\Delta f = -15$ Hz. (e) Image after repeated manipulation attempt at $\Delta f = -75$ Hz. The purple nanoribbon remains at its position. Frequency shift used for imaging $\Delta f = -15$ Hz. (f) Comparison of the position of the red nanoribbon before and after manipulation. The black profile shows the graphene nanoribbon in its original position. For all images $c_L = 37$ N/m, $f_0 = 331$ Hz, $A = 6$ nm, and $Q = 24\,000$.

Figure 3(a) shows two other graphene nanoribbons to be manipulated marked in different colors. The red graphene nanoribbon appears noisy and is weakly bound to the substrate. The purple graphene nanoribbon is bound to a neighboring nanoribbon and stabilized by this bond. Additional structures have been marked in green as a guide to the eye. The manipulation protocol is similar to the one described above. The yellow circle in Fig. 3(a) marks the starting point and the blue arrow shows the direction and endpoint of the manipulation path.

Figure 3(b) shows an enlarged view of the graphene nanoribbons to be manipulated. In this image the surface bonding of different strength of the red and purple nanoribbon becomes particularly clear due to the strongly smeared edges of the red nanoribbon. The purple nanoribbon is bound more strongly but it is connected to the other graphene nanoribbons only at one position marked by a red circle. The goal of the manipulation experiment was to move the purple graphene nanoribbon in the direction of the structure marked in green and to break the bond. The manipulation path has been chosen to be longer to manipulate also the nanoribbon marked in red, which is weakly bound. The frequency set-point is set to $\Delta f = -60$ Hz at the start of the manipulation. The white lines in Figs. 3(b) and 3(d) show the position of the height profiles depicted in Fig. 3(f). In Fig. 3(c) the red and the purple nanoribbons are still located at their original position.

In the course of the manipulation experiment, Δf is lowered to -60 and -75 Hz. The results are shown in Figs. 3(c) and 3(d). The purple nanoribbon remains in its original position whereas the red nanoribbon has moved from the nanoribbon marked in green on the right hand side to the nanoribbon marked in green on the left hand side. The line profiles taken before and after manipulation [Fig. 3(f)] confirm the displacement of the red nanoribbon by 1.8 nm, a distance that is clearly distinct from the smallest relevant length scale in the Au(111) herringbone reconstruction: The distance between elevated areas separated by a hexagonal close-packed region is 2.4 nm; see Ref. [45]. Another manipulation attempt at the same frequency shift does not lead to further changes [Fig. 3(e)].

For both manipulation events discussed in this work Figs. 1 and 3, large oscillation amplitudes are used. From the overall geometry of the process, for the manipulation shown in Fig. 1, it seems unlikely that the tip should remain in permanent contact to the nanoribbon during the manipulation process: Since the oscillation amplitude is 6 nm and the length of the nanoribbon is about 15 nm, maintaining a permanent contact to the tip during one oscillation cycle would mean to displace the nanoribbon by 12 nm (two times the oscillation amplitude) along its length for the experiment shown in Fig. 1. It would then form a 12-nm free-standing chord; see Fig. 4(a). In the state detached from the surface, the nanoribbon would shake thermally and it would be unlikely that it is placed back to a position where the center of the ribbon has precisely the same position with respect to a neighboring short ribbon discussed as the turning point of the manipulation process above. We therefore think that it is more realistic that the nanoribbon remains near the surface, as shown in the extreme case in Fig. 4(b). In alignment with these considerations we consider the manipulation event to have a short time duration on the timescale of the cantilever oscillation, similar to a collision event. When small oscillation amplitudes are used, it could be that several collision events lead to the final movement as in a stick-slip motion while the GNR remains attached to the tip. Here, we can exclude such stick-slip motion from the details of our experimental setup due to using large oscillation amplitudes.

For the experiment shown in Fig. 3, lifting the nanoribbon with the tip could mean to fold it, since the tip is positioned near the center of the nanoribbon [Fig. 4(c)]. The tip touches

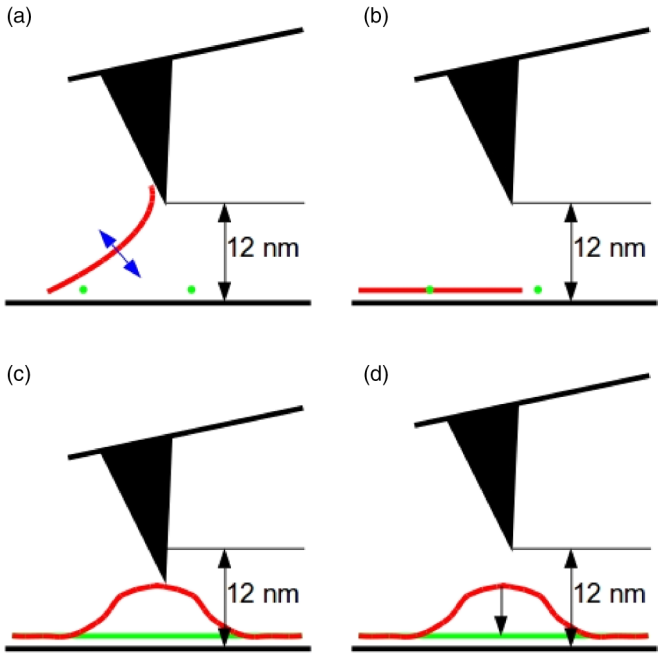

FIG. 4. Situation near the upper turning point of the oscillation. (a), (b) Possible scenarios during manipulation of the graphene nanoribbon shown in Fig. 1. In panel (a) the situation is shown, where the tip remains in contact with the nanoribbon during a full oscillation cycle. This situation is unlikely, because the nanoribbon is placed back to its original position rather precisely. Panel (b) shows a more realistic scenario, where the tip does not lift the nanoribbon during manipulation. (c), (d) Possible scenarios during manipulation of the graphene nanoribbon shown in Fig. 3(c) The tip partly lifts the nanoribbon, but panel (d) does not remain in contact at the upper turning point of the oscillation. This is in agreement with the displacement of the nanoribbon along its length observed in this experiment.

the ribbon only 15 nm from its end near the lower left corner of the image and about 10 nm away from a kink near the top right end of the ribbon. Remaining in permanent contact would mean that the ribbon were nearly completely detached from the surface at the upper turning point of the oscillation. It seems unlikely that a folded and/or largely detached nanoribbon would be automatically placed back in such a precise way. For this manipulation experiment, the nanoribbon is not only moved in the direction perpendicular to the GNR by 1.8 nm but it is also moved along its length by about 5 nm. This can best be confirmed by comparing the position of the kink in the red nanoribbon in Fig. 3(a) to the position of the kinks in the green nanoribbons, and by doing the same comparison for Fig. 3(e). Here, the motion of the nanoribbon along its length is guided by the neighboring green nanoribbons on the surface. We conclude that it is unlikely that the tip remains in permanent contact to the nanoribbon while it moves laterally, but that it is likely that part of the nanoribbon is lifted for several nanometers during the manipulation event which probably takes place within only one oscillation cycle. The geometry during lifting is described schematically in Fig. 4(c).

Several theoretical proposed mechanisms of molecular manipulation have been compared to experimental

results concerning 3,4,9,10-Perylene-tetracarboxylicacid-dianhydride (PTCDA) manipulation on the Ag(111) surface at 5 K using small oscillation amplitudes (0.4 nm) [16]. It has been proposed that the motion of the molecule could span as large as 4 lattice spacings due to the transfer of potential energy from the tip to the molecule, allowing the molecule to perform long jumps. Here, also a manipulation mechanism explains best the experimental results, where during one tip-sample contact event energy is transferred from the tip to the sample, because the nanoribbon is never imaged in an excited state. This result could be discussed in relation to experiments where nanoribbons were displaced along their length over distances of more than 1 nm in one sliding event [10]. Applying these considerations to the manipulation experiments shown here, we think that by lifting a nanoribbon a sufficiently large amount of potential energy could be transferred for the nanoribbon to be displaced over several lattice positions. Here, we displace the nanoribbon in a controlled way in the direction perpendicular to its length, but we can show that by the interaction with the tip it is additionally moved along its length. This allows us to separate the effect of mechanically pushing the nanoribbon from the effect of lifting it. While lifting the nanoribbon occurs while the nanoribbon is in contact with the tip, pushing it to the side could occur by momentum transfer, because the tip does not remain in contact with the nanoribbon until it has reached its final position.

IV. THEORETICAL PART

In the following, we investigate possible reasons for the loosely bound GNRs using periodic DFT calculations. Our analysis focuses on determining translation barriers, which provide insight into the strength of the GNR–surface interaction. We also examine different orientations of the GNRs relative to the surface, as the initial experiments showed that a slight rotation increases their stability.

A. Adsorption orientations

The purpose of our theoretical calculations is to determine approximate translation barriers for GNRs adsorbed in different orientations with respect to the Au(111) surface. Therefore, we start from optimized lattice constants of $a_{\mathrm{Au}} = 2.897\,\text{Å}$ and $a_{\mathrm{GNR}} = 4.290\,\text{Å}$. Using these values of a_{Au}, a_{GNR}, we have identified orientations of the GNR, which lead to nearly commensurate translation vectors along the direction parallel to the GNR. Additionally, we take only orientations which lead to unit cells of reasonable size. Details are given in the Appendix B. In this way, we identify three further adsorption orientations B, C, and D in addition to the one reported in Ref. [38], labeled as A in the following. In other works A is given as R30 [46]. A sketch of these orientations is given in Figs. 5(a) and 5(b) the unit cells used for the periodic calculations are indicated. The unit cells for the different orientations contain different numbers of GNR repeat units, n_{GNR}, i.e., $n_{\mathrm{GNR}} = 2$ (A), $n_{\mathrm{GNR}} = 3$ (B), $n_{\mathrm{GNR}} = 6$ (C), and $n_{\mathrm{GNR}} = 5$ (D).

To identify suitable adsorption geometries for the orientations B, C, and D, a rough scan of possible lateral positions of the GNR with respect to the primitive surface unit cell was

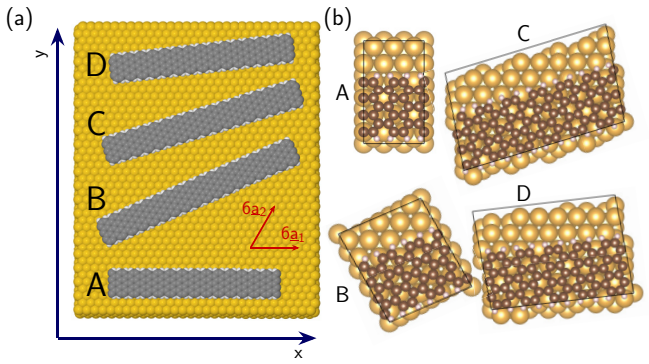

FIG. 5. (a) Schematic representation the different adsorption orientations considered in this investigation (A, B, C, and D). The Cartesian coordinate system is indicated by the blue arrows, the directions of the primitive surface unit cell vectors, $\underline{a}_1$ and $\underline{a}_2$ by the red arrows. (b) Top view on the optimized adsorption geometries for all orientations. The unit cells for the periodic calculations are indicated by black lines.

done before the actual geometry optimization. Top views of the optimized geometries are shown in Fig. 5(b). The unit cell vectors chosen with respect to the optimized Au bulk lattice and the coordinates of the lowest Au layer in the slab are kept fixed in these optimizations. The binding energies normalized with respect to n_{GNR} are comparable for all orientations, i.e., 1.26 eV (A), 1.13 eV (B), 1.31 eV (C), and 1.21 eV (D). Further, for all orientations the planar geometry of the GNR is slightly bent in a way that the outer carbon and hydrogen atoms are closer to the surface than the inner carbon atoms. Further details about the geometry optimization are given in the Appendixes A–C.

B. Translation barriers and frequencies

Translation barriers have been calculated using two approaches. In the first approach, we generate a 2D translation potential energy surface by rigidly translating the GNR along the gold surface unit vectors. This potential has then been extended periodically to represent the full surface. We have applied this procedure to all four GNR orientations, allowing us to extract the corresponding translational energy barriers as well as the directions in which these barriers occur. We have then performed CI-NEB calculations over the previously defined barriers. We choose these two complementary approaches because, in a realistic scenario, the GNR will undergo atomic relaxation during translation. However, this relaxation is unlikely to be complete, as the timescale of translation may fall short of that needed for structural reorganization. By comparing the rigid 2D potential with the fully relaxed CI-NEB pathway, we establish upper and lower bounds for the actual energy barrier. The true energy cost of translation is expected to lie between these two limiting cases.

We calculate approximate translation potentials, i.e., potentials for the motion of the whole GNR along coordinates x and y [cf. Fig. 5(a)], starting from the optimized geometries for each orientation. Here, we choose the following approach: (i) The internal geometry of the GNR is kept rigid and at constant height, i.e., fixed z coordinate for all atoms. Then,

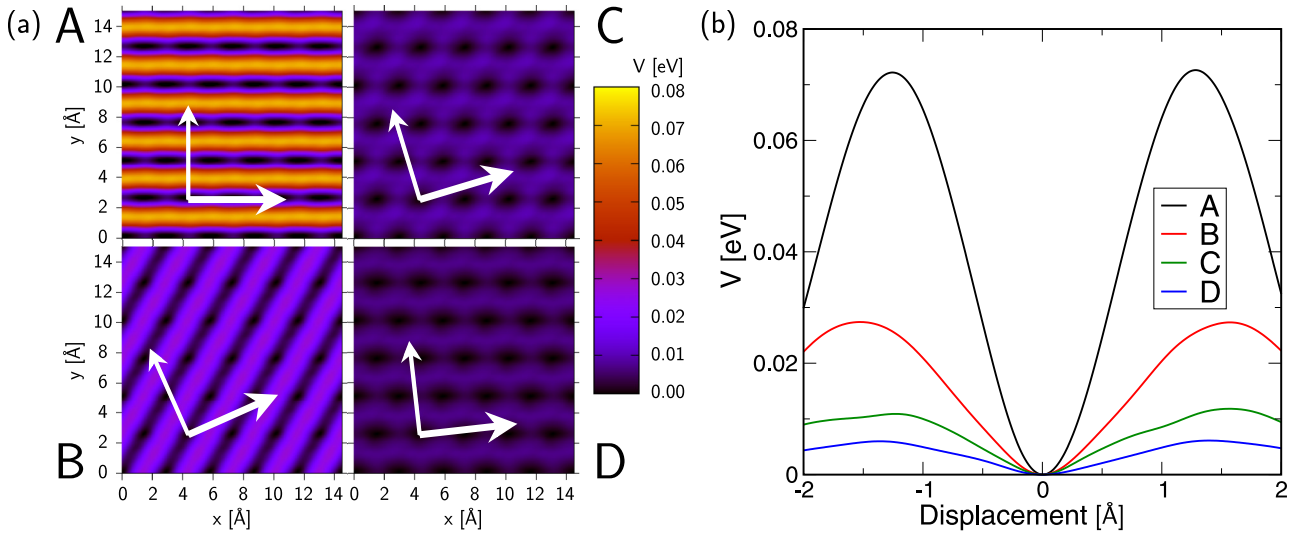

FIG. 6. (a) Translation potentials for the lateral displacement of the rigid GNR along x and y [cf. Fig 5(a)] over a gold slab (details see text). The direction parallel to the GNR is indicated by the gray arrow, the on perpendicular to the GNR by the white arrow. (b) One-dimensional cuts of the potentials along the direction perpendicular to the GNR. All potentials are normalized with respect to n_{GNR}.

the whole GNR is translated along $\underline{a}_1$ and $\underline{a}_2$ [cf. Fig. 5(a)] in the primitive surface unit cell. (ii) The surface Au layers are kept fixed in positions where the x and y coordinates correspond to the values derived from the optimized geometry, while the z coordinate is set to the average z coordinate of each layer obtained for the optimized geometry. As a result we get translation potentials which are almost periodic with respect to the primitive surface unit cell. To obtain the periodic potentials, a 2D fourier interpolation is done. We use seven discrete points along $\underline{a}_1$ and $\underline{a}_2$, i.e., 49 points in total to calculate the translation potential. Figure 6(a) shows the Fourier interpolated potential as a function of the translation of the GNR along x and y [see Fig. 5(a)] for the different orientations (details about the interpolation are given in the Appendix D). The directions parallel to the GNRs are indicated by the thick arrows, the ones perpendicular to the GNRs by the thin arrows. In Fig. 6(b), one can see one-dimensional cuts through the potential along the perpendicular direction. The potentials are given relative to the minimal adsorption energy and are normalized with respect to n_{GNR}. A small shift of the minimum position occurs, due the Fourier interpolation and the changed Au coordinates, compared to the optimized geometry given in Fig. 5(b). These shifts are equal or less 0.1 Å and are corrected in Fig. 6(b) for a better comparison between the different orientations. Further, test calculations for orientation A show that the barriers obtained in this way are in the same order of magnitude as the ones one obtained translating the rigid GNR with respect to the optimized rigid surface.

In the CI-NEB approach, we have proceeded as follows: (i) we have identified a surface vector along which the GNR exhibits a notable energy barrier in the 2D potential, (ii) we have translated the relaxed GNR geometry by one unit cell along this direction and re-optimized the resulting structure, (iii) we have used the initial and final configurations as endpoints in a CI-NEB calculation to determine the minimum energy path and the associated barrier.

We have applied this procedure to all orientations. The resulting energy barriers vary between orientations, as summarized in Table I. The same qualitive trend compared with the approximate translation potentials is observed. The corresponding translation vectors are visualized in Fig. 7, which illustrates as well the CI-NEB energy profiles.

These findings support the assumption that the true energy barrier lies between the two limiting cases represented by the rigid 2D potential and the fully relaxed CI-NEB path.

Looking at Fig. 6 one immediately recognizes that the translation potentials are quite different for the different orientations although the binding energies are comparable. The initial barriers for a translation in the direction perpendicular to the GNR, i.e., the energies of the first potential maxima along this direction, are given in Table I. Here, A has by far the largest translation barrier, while D exhibits the smallest, which is approximately 12 times smaller. In the CI-NEB calculation, this difference is even greater, with the barrier being about 25 times smaller.

To compare to the experimental hopping rates (see above), we have additionally computed the second derivative of the one-dimensional potential cut at the minimum, k_{prep}. We use the mass of one GNR repeat unit ($C_{14}H_4$, 172.19 amu) to obtain harmonic frequencies ν_{harm}. These values can also be found in Table I. Taking these frequencies as the Arrhenius prefactor, one can estimate the hopping rate as a function of the GNR length, l_{GNR}, as

$$\gamma = \nu_{\mathrm{harm}} \exp\left(-\frac{l_{\mathrm{GNR}}\Delta V}{a_{\mathrm{GNR}} k_B T}\right). \tag{1}$$

From Eq. (1), it follows

$$l_{\mathrm{GNR}} = -\ln\left(\frac{\gamma}{\nu_{\mathrm{harm}}}\right)\frac{a_{\mathrm{GNR}} k_B T}{\Delta V}. \tag{2}$$

We note that the barrier heights ΔV obtained from the translation potential are likely overestimated, while the harmonic frequencies ν_{harm} are probably underestimated. This implies

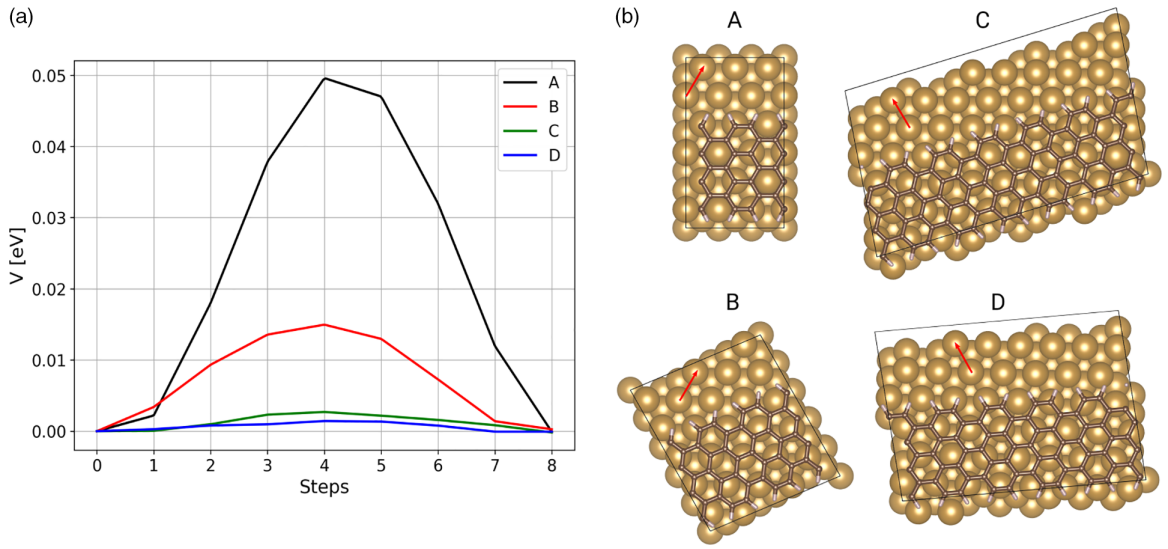

FIG. 7. (a) CI-NEB Path for the different orientations normalized per anthrylene unit energies. (b) The different orientations and the direction of the CI-NEB presented by the red arrow.

that the theoretically predicted hopping rates likely underestimate the actual mobility of the GNRs. Conversely, the CI-NEB barriers tend to underestimate ΔV, which would lead to an overestimation of mobility.

Since l_{GNR} depends reciprocally on ΔV but only logarithmically on ν_{harm}, errors in ΔV have a much stronger impact on the predicted GNR length than errors in ν_{harm}. This highlights the dominant role of the barrier height in controlling GNR mobility.

The lower bound of experimental hopping rates at 298.15 K was determined to be 1 s^{-1} (see above). This corresponds to predicted GNR lengths of 4 nm (A), 11 nm (B), 27 nm (C), and 48 nm (D) for the translation potential barriers, and 6 nm (A), 20 nm (B), 162 nm (C), and 125 nm (D) for the CI-NEB barriers.

These characteristic lengths provide a natural explanation for the "fuzzy" appearance of structures B, C, and D in STM images. In these cases, the GNRs are sufficiently short to enable thermally activated motion along the surface perpendicular to the length of the GNR. Because the effective barrier scales with l_{GNR}, longer nanoribbons exhibit more restricted movement in this direction—yet still retain enough mobility to appear fuzzy. Conversely, orientation A becomes immobile at much shorter lengths, effectively freezing the GNR in place.

Notably, D deviates by only 6° from A (16° for C), indicating that even small changes in orientation can significantly alter the mobility even though the binding energies of the configurations are similar within the precision of the calculation methods. In the case of B, the rotation angle of 24° matches the experimental value, suggesting that a transition from orientation B to A may have been directly observed.

V. SUMMARY

Using SFM, we have imaged GNRs on Au(111) and have observed a variety of configurations, including freestanding ribbons, interconnected networks, and point-wise junctions. The orientation of GNRs has consistently occurred at approximately 60° from one another, which reflects the sixfold rotational symmetry (C_6) of the Au(111) surface. In several cases, we have observed a fuzzy appearance of the ribbons, indicative of dynamic fluctuations or hopping between nearby adsorption sites. These observations have motivated a detailed theoretical analysis of the underlying adsorption orientations and energy barriers.

We have identified four nearly isoenergetic adsorption orientations (A–D) based on DFT calculations. To estimate and compare their translational energy barriers, we have applied two complementary approaches: a two-dimensional potential energy surface scan without atomic relaxation, and NEB calculations with full relaxation. Orientation A has shown the highest kinetic stability, featuring the largest energy barrier and the correspondingly shortest critical length—that is, the maximum ribbon length below which thermal fluctuations and SFM tip interactions can induce motion. Compared to B, the next most stable orientation, A exhibits a barrier about three times higher, resulting in a critical length roughly three times shorter. This kinetic profile aligns well with the experimental observations: GNRs that appear fuzzy in SFM images are typically shorter than the calculated critical length and can switch between nearby minima, particularly in orientations B–D, which exhibit lower barriers. In contrast, GNRs longer than the critical length remain localized in a single minimum and thus appear sharp—regardless of orientation. Notably, since orientation A has the shortest critical length, even relatively short ribbons can remain stable in this configuration. The experimentally observed fuzzy GNRs have lengths of approximately 10–40 nm, while the theoretically predicted critical lengths range from about 15 nm to over 100 nm depending on orientation, indicating not only qualitative but also good quantitative agreement. However, it should be noted that since PBE tends to underestimate energy barriers, the actual critical lengths may be somewhat shorter than predicted.

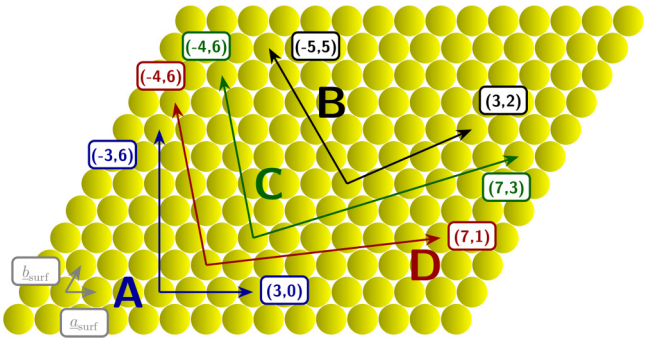

FIG. 8. Unit cells for the different orientations of the gold (111)-surface.

We conducted SFM manipulation experiments on freestanding GNRs by moving the tip perpendicular to the ribbon axis. In the first experiment, we observed a rotation of about 24°, which could correspond to a transition from orientation B to A, as these orientations differ by exactly this angle. Attempts to manipulate GNRs connected to others at their ends were unsuccessful, indicating increased stability. In a separate experiment, we were able to translate a freestanding GNR by moving the tip perpendicular to its length and gradually increasing the tip frequency until motion occurred. This observation is consistent with our calculated energy barriers. Additionally, motion along the length of the GNR was occasionally observed, which can be explained by the near absence of an energy barrier in this direction in our calculations and by partial lifting of the GNR during the oscillation cycle of the tip.

ACKNOWLEDGMENTS

We thank H. von Löhneysen for enlightening discussions and C. Pérez León and M. Marz for their support with the experimental work. This work was supported by the ERC Starting Grant NANOCONTACTS (No. 239838) and by the German Research Foundation (DFG) within the framework of the Collaborative Research Center (CRC) 1636–Project No. 510943930, Project A07.

DATA AVAILABILITY

The data that support the findings of this article are openly available [47].

APPENDIX A: COMPUTATIONAL DETAILS

All calculations in this work were performed using VASP [31,32,48]. The projector-augmented wave (PAW) [33,34] method was employed together with the PBE exchange-correlation functional [35] and dispersion corrections via Grimme D3 with Becke–Johnson damping [36]. A plane-wave cutoff energy of 400 eV was used for all calculations. Following the setup reported in Ref. [38], we used a Γ-centered k-point mesh of (16, 16, 16) for bulk gold and (6, 1, 1) for the isolated GNR. For the combined systems, the following k-point meshes were used: orientation A: (4, 4, 1), B: (2, 4, 1), C: (1, 4, 1), and D: (1, 4, 1). Default convergence criteria were applied. Nonspherical gradient corrections within the PAW spheres were included by setting `LASPH =.TRUE.`. For large unit cells, particularly those combining the ribbon and the surface, we enabled `LREAL =.AUTO.` to optimize performance.

APPENDIX B: ORIENTATIONS

To construct the different orientations: We use a hexagonal lattice for the surface, which is assumed to be in the *xy* plane. The second coordinate is omitted in the following, i.e.,

$$\underline{a}_{\text{surf}} = a_{\text{Au}} \begin{pmatrix} 1 \\ 0 \end{pmatrix}, \tag{B1}$$

$$\underline{b}_{\text{surf}} = a_{\text{Au}} \begin{pmatrix} \frac{1}{2} \\ \frac{1}{2}\sqrt{3} \end{pmatrix}. \tag{B2}$$

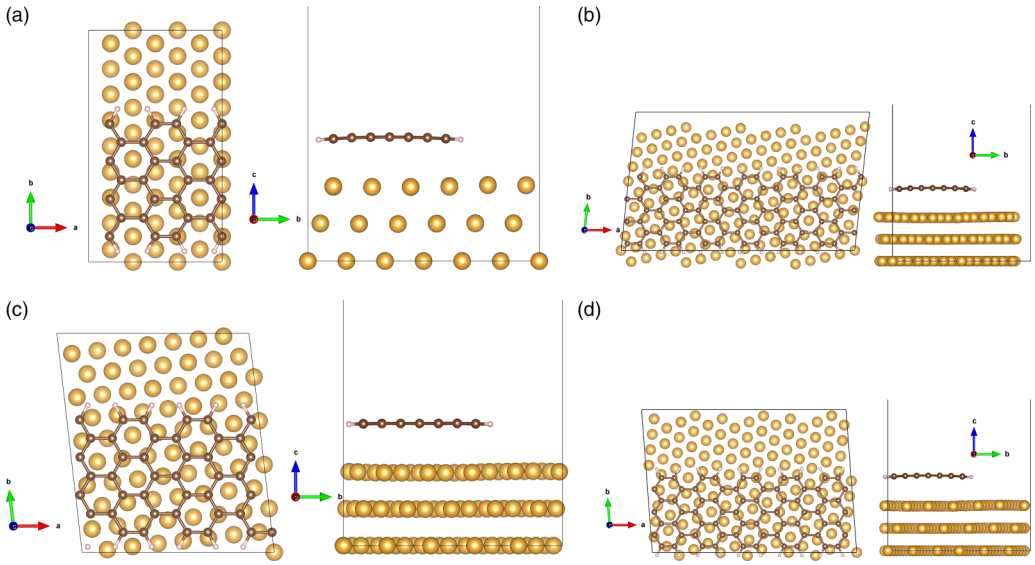

FIG. 9. Shown are the optimized geometries and unit cells for all adsorption orientations aswell the bending of the GNR on the edges is shown.

TABLE II. Length of the GNR in different orientations under varying conditions, given in nanometers.

	$\Delta V_{\text{2D Potential}}$		$\Delta V_{\text{CI-NEB}}$	
Orientation	$T = 115$ K	$T = 298.15$ K	$T = 115$ K	$T = 298.15$ K
A	1.6 nm	4.1 nm	2.3 nm	6.0 nm
B	4.1 nm	10.7 nm	7.6 nm	19.6 nm
C	10.3 nm	26.8 nm	62.5 nm	162.2 nm
D	18.5 nm	48.0 nm	48.2 nm	124.9 nm

The ratio r between the two different lattice constants is

$$r = \frac{a_{\text{Rib}}}{a_{\text{Au}}} = 1.48054. \tag{B3}$$

We need to identify suitable total units cells

$$\underline{A} = k_a \underline{a}_{\text{surf}} + k_b \underline{b}_{\text{surf}}, \quad k_a, k_b \in \mathcal{Z}, \tag{B4}$$

$$\underline{B} = l_a \underline{a}_{\text{surf}} + l_b \underline{b}_{\text{surf}}, \quad l_a, l_b \in \mathcal{Z}, \tag{B5}$$

with $|\underline{A}| \approx n_{\text{Rib}} a_{\text{Rib}}$, $n \in \mathcal{Z}$. We further demand $k_a, k_b < 10$. We define a scaling factor subject to the following condition:

$$f_{\text{scale}} = \frac{|\underline{A}|}{n_{\text{Rib}} a_{\text{Rib}}}, \quad f_{\text{scale}} \in [0.98 : 1.02]. \tag{B6}$$

In what follows we use the notation

$$\underline{A} = k_a \underline{a}_{\text{surf}} + k_b \underline{b}_{\text{surf}} = (k_a, k_b),$$

the same for $\underline{B}$. Using these conditions we identify the following orientation, for which we use the k-point grids as follows:

(1) $(3,0) \times (-3,6)$, $n_{\text{Rib}} = 2$, k-point grid (6,4,1),
(2) $(3,2) \times (-5,5)$, $n_{\text{Rib}} = 3$, k-point grid (4,4,1),
(3) $(7,1) \times (-4,6)$, $n_{\text{Rib}} = 5$, k-point grid (2,4,1),
(4) $(7,3) \times (-4,6)$, $n_{\text{Rib}} = 6$, k-point grid (2,4,1).

The gold unit cells corresponding to the different orientations A, B, C, and D are shown in Fig. 8. The bending of the GNR on the gold surface, as discussed in the main text, is illustrated in Fig. 9. The length of the GNR in different orientations is given in Table II. The corresponding POSCAR files for these structures are provided in Zenodo at Ref. [47].

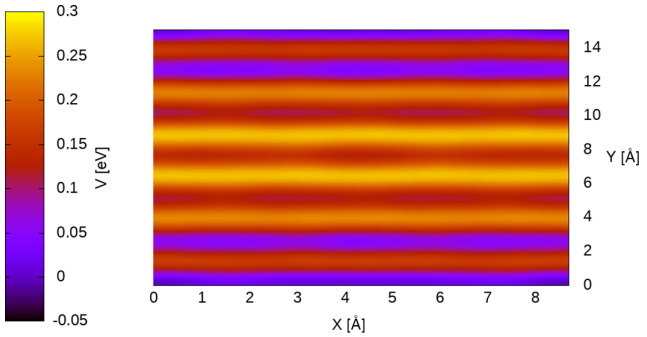

FIG. 10. Fourier interpolated PES for translation of the rigid ribbon over the rigid surface starting from the optimized geometry covering the total unit cell A.

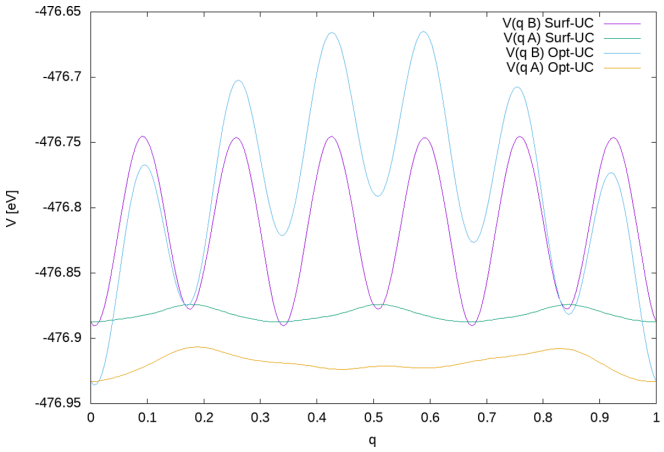

FIG. 11. One-dimensional cuts along $\underline{A}$ and $\underline{B}$ of the translation PES for A. Opt-UC is for translation of the rigid ribbon over the rigid surface starting from the optimized geometry covering the total unit cell. Surf-UC is based on a translation of the rigid ribbon with optimized coordinates and the surface layers with averaged z coordinates, where only on surface unit cell is considered.

APPENDIX C: CONVERGENCE TESTS

Convergence tests were performed to determine the appropriate vacuum thickness and the number of gold layers (slabs) to be used. As a test system, we selected the simplest orientation A for convenience. The number of slabs was varied from 3 to 5, and the vacuum spacing was varied between 15 and 19 Å. For all resulting structures, we computed the binding energy as follows:

$$\Delta E_{\text{b}} = E_{\text{opt}} - E_{\text{surf}} - E_{\text{rib}}. \tag{C1}$$

In the following, we define the binding energy per ribbon unit cell as $\delta E = \Delta E_{\text{b}}/n_{\text{rib}}$ denotes the number of ribbon unit cells included in the simulation supercell. For the convergence tests, we used $n_{\text{rib}} = 2$, which corresponds to the $(3,0) \times (-3.6)$ supercell. The results of the convergence tests are summarized in Table III. As can be seen, the chosen settings provide reasonable convergence, taking into account the typical uncertainties associated with translational energy barriers in static calculations. All calculations presented in this work were performed using a vacuum spacing of 15 Å and three layers of gold.

Further, it should be noted that the bonding of the GNR to the surface is mainly due to dispersion forces and a small charge transfer between the GNR and the surface. In Ref. [19], we performed extensive convergence tests for **A** with respect

TABLE III. Convergence tests for different binding energies (details see text, all values in eV).

Parameters	δE
3 layer, $z_{\text{vac}} \approx 15$ Å	1.2628
3 layer, $z_{\text{vac}} \approx 17$ Å	1.2620
3 layer, $z_{\text{vac}} \approx 19$ Å	1.2643
4 layer, $z_{\text{vac}} \approx 15$ Å	1.3133
5 layer, $z_{\text{vac}} \approx 15$ Å	1.3176

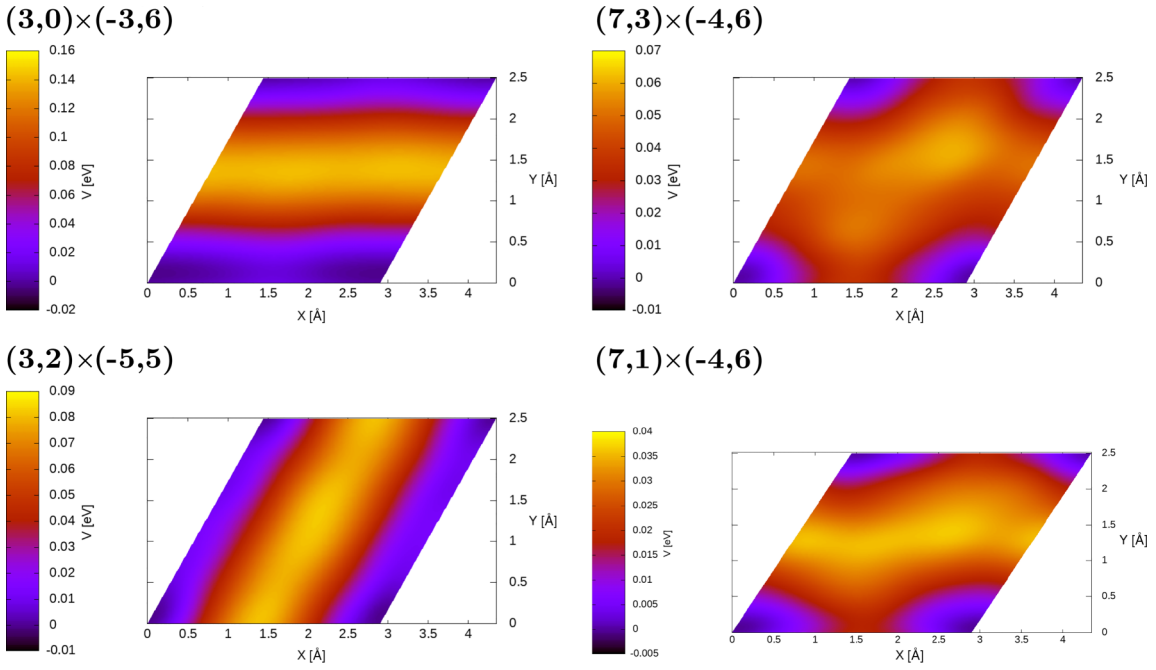

FIG. 12. PES for translation potentials using the surface unit cell and averaged z positions for the Au atoms (details see text). Shown are the PES for a single surface unit cell.

to the calculation of local contact potential difference maps. In these calculations, we used slabs containing up to seven layers and found that both the local potential and the adsorption geometry are converged for the three-layer system. This indicates that the charge transfer is correctly described in the three-layer system. Since the bonding situation does not fundamentally change when the GNR moves laterally, this conclusion should also apply to the whole PES.

APPENDIX D: TRANSLATIONAL BARRIERS

For the smallest system a translation of the rigid ribbon over the rigid surface for the whole optimized system unit cell was performed. We use 21 equidistant points along $\underline{A}$ and 37 along $\underline{B}$. The resulting PES (Fourier interpolated) is shown in Fig. 10

As one can see, the surface unit cell is still "visible." This becomes more clearly in one-dimensional cuts along $\underline{A}$ and $\underline{B}$ shown in Fig. 11 (Opt-UC). Also shown here, are the same cuts for a PES based on a translation of the rigid ribbon with optimized coordinates and the surface layers with averaged z coordinates (Surf-UC). Here, only the surface unit cell is sampled. Both assumptions are somewhat arbitrary, but as both qualitatively agree and are in line to the scans shown in Fig. 12, where the sampling over the unit cells of gold from each orientation is shown as described in the paper. But here only presented for one unit vector along a and b of gold and not a larger section as we did it in the paper.

APPENDIX E: NUDGED ELASTIC BAND

The CI-NEB method [49] was employed to investigate the translational motion of GNR molecules on the surface. All calculations were performed using VASP, with the support of the VTST tools provided by the Henkelman group, which were used to generate a total of seven intermediate images along the reaction path. For the geometries prepared for the NEB calculations, stricter convergence criteria were required, so we chose 10^{-6} eV for electronic convergence in the SCF-cycle and 10^{-4} eV/Å as the maximum energy difference between a step, respectively. The path optimization was carried out using the fast inertial relaxation engine algorithm [50] with standard settings. A spring constant of $-5\,\mathrm{eV/Å^2}$; was used, and the convergence criterion for the atomic forces was set to 0.02 eV/Å. The transition state was identified as the image with the highest energy along the minimum energy path.

APPENDIX F: CHARACTERISTIC LENGTHS

We used Eq. (2) to calculate the immobile length of the GNR the length at which the GNR becomes static on the surface due to translation barriers. These values were determined for the two temperature extremes given in the experimental part and are reported for both calculated potentials.

[1] D. M. Eigler and E. K. Schweizer, Positioning single atoms with a scanning tunneling microscope, Nature (London) **344**, 524 (1990).

[2] J. A. Stroscio and D. M. Eigler, Atomic and molecular manipulation with the scanning tunneling microscope, Science **254**, 1319 (1991).

[3] R. Lüthi, E. Meyer, H. Haefke, L. Howald, W. Gutmannsbauer, and H.-J. Güntherodt, Sled-type motion on the nanometer scale: Determination of dissipation and cohesive energies of C_{60}, Science **266**, 1979 (1994).

[4] P. E. Sheehan and C. M. Lieber, Nanotribology and nanofabrication of MoO_3 structures by atomic force microscopy, Science **272**, 1158 (1996).

[5] N. Oyabu, O. Custance, I. Yi, Y. Sugawara, and S. Morita, Mechanical vertical manipulation of selected single atoms by soft nanoindentation using near contact atomic force microscopy, Phys. Rev. Lett. **90**, 176102 (2003).

[6] M. Ternes, C. P. Lutz, C. F. Hirjibehedin, F. J. Giessibl, and A. J. Heinrich, The force needed to move an atom on a surface, Science **319**, 1066 (2008).

[7] C. Wagner, N. Fournier, F. S. Tautz, and R. Temirov, Measurement of the binding energies of the organic-metal perylene-teracarboxylic-dianhydride/Au(111) bonds by molecular manipulation using an atomic force microscope, Phys. Rev. Lett. **109**, 076102 (2012).

[8] F. J. Giessibl, Atomic resolution of the silicon (111)-(7 × 7) surface by atomic force microscopy, Science **267**, 68 (1995).

[9] S. Kitamura and M. Iwatsuki, Observation of 7 × 7 reconstructed structure on the Silicon (111) surface using ultrahigh-vacuum noncontact atomic force microscopy, Jpn. J. Appl. Phys. **34**, L145 (1995).

[10] S. Kawai, A. Benassi, E. Gnecco, H. Söde, R. Pawlak, X. Feng, K. Müllen, D. Passerone, C. A. Pignedoli, P. Ruffieux, R. Fasel, and E. Meyer, Superlubricity of graphene nanoribbons on gold surfaces, Science **351**, 957 (2016).

[11] S. Kawai, A. S. Foster, F. F. Canova, H. Onodera, S. Kitamura, and E. Meyer, Atom manipulation on an insulating surface at room temperature, Nat. Commun. **5**, 4403 (2014).

[12] Y. Sugimoto, P. Jelinek, P. Pou, M. Abe, S. Morita, R. Perez, and O. Custance, Mechanism for room-temperature single-atom lateral manipulations on semiconductors using dynamic force microscopy, Phys. Rev. Lett. **98**, 106104 (2007).

[13] S. Torbrügge, O. Custance, S. Morita, and M. Reichling, Manipulation of individual water molecules on CeO_2 (111), J. Phys.: Condens. Matter **24**, 084010 (2012).

[14] Y. Sugimoto, M. Abe, S. Hirayama, N. Oyabu, O. Custance, and S. Morita, Atom inlays performed at room temperature using atomic force microscopy, Nat. Mater. **4**, 156 (2005).

[15] I. Yi, R. Nishi, M. Abe, Y. Sugimoto, and S. Morita, Lateral manipulation of single defect on insulating surface using non-contact atomic force microscope, Jpn. J. Appl. Phys. **50**, 015201 (2011).

[16] G. Langewisch, J. Falter, A. Schirmeisen, and H. Fuchs, Long jumps of an organic molecule induced by atomic force microscopy manipulation, Adv. Materials Inter. **1**, 1300013 (2014).

[17] Z. Chen, Y.-M. Lin, M. J. Rooks, and P. Avouris, Graphene nano-ribbon electronics, Physica E **40**, 228 (2007).

[18] M. Y. Han, B. Özyilmaz, Y. Zhang, and P. Kim, Energy band-gap engineering of graphene nanoribbons, Phys. Rev. Lett. **98**, 206805 (2007).

[19] D. Rothhardt, A. Kimouche, T. Klamroth, and R. Hoffmann-Vogel, Local work function on graphene nanoribbons, Beilstein J. Nanotechnol. **15**, 1125 (2024).

[20] S. Schneider and R. Hoffmann-Vogel, Electrostatic forces above graphene nanoribbons and edges interpreted as partly hydrogen-free, Nanoscale **12**, 17895 (2020).

[21] M. Koch, F. Ample, C. Joachim, and L. Grill, Voltage-dependent conductance of a single graphene nanoribbon, Nat. Nanotechnol. **7**, 713 (2012).

[22] J. Björk, S. Stafstrom, and F. Hanke, Zipping up: Cooperativity drives the synthesis of graphene nanoribbons, J. Am. Chem. Soc. **133**, 14884 (2011).

[23] S. Blankenburg, J. Cai, P. Ruffieux, R. Jaafar, D. Passerone, X. Feng, K. Müllen, R. Fasel, and C. A. Pignedoli, Intraribbon heterojunction formation in ultranarrow graphene nanoribbons, ACS Nano **6**, 2020 (2012).

[24] C. Ma, Z. Xiao, H. Zhang, L. Liang, J. Huang, W. Lu, B. G. Sumpter, K. Hong, J. Bernholc, and A.-P. Li, Controllable conversion of quasi-freestanding polymer chains to graphene nanoribbons, Nat. Commun. **8**, 14815 (2017).

[25] Z. Xiao, C. Ma, W. Lu, J. Huang, L. Liang, K. Hong, A.-P. Li, B. G. Sumpter, and J. Bernholc, *Ab initio* investigation of the cyclodehydrogenation process for polyanthrylene transformation to graphene nanoribbons, npj Comput. Mater. **5**, 91 (2019).

[26] C. Ma, Z. Xiao, P. V. Bonnesen, L. Liang, A. A. Puretzky, J. Huang, M. Kolmer, B. G. Sumpter, W. Lu, K. Hong, *et al.*, On-surface cyclodehydrogenation reaction pathway determined by selective molecular deuterations, Chem. Sci. **12**, 15637 (2021).

[27] L. Gigli, S. Kawai, R. Guerra, N. Manini, R. Pawlak, X. Feng, K. Müllen, P. Ruffieux, R. Fasel, E. Tosatti, *et al.*, Detachment dynamics of graphene nanoribbons on gold, ACS Nano **13**, 689 (2019).

[28] R. Li and F. Xu, Competition between sliding and peeling of graphene nanoribbons under horizontal drag, Materials **15**, 3284 (2022).

[29] J. Cai, P. Ruffieux, R. Jaafar, M. Bieri, T. Braun, S. Blankenburg, M. Muoth, A. P. Seitsonen, M. Saleh, X. L. Feng, K. Müllen, and R. Fasel, Atomically precise bottom-up fabrication of graphene nanoribbons, Nature (London) **466**, 470 (2010).

[30] S. Schneider, K. Bytyqi, S. Kohaut, P. Bügel, B. Weinschenk, M. Marz, A. Kimouche, K. Fink, and R. Hoffmann-Vogel, Molecular self-assembly of DBBA on Au(111) at room temperature, Phys. Chem. Chem. Phys. **24**, 28371 (2022).

[31] G. Kresse and J. Furthmüller, Efficiency of *ab-initio* total energy calculations for metals and semiconductors using a plane-wave basis set, Comput. Mater. Sci. **6**, 15 (1996).

[32] G. Kresse and J. Furthmüller, Efficient iterative schemes for *ab initio* total-energy calculations using a plane-wave basis set, Phys. Rev. B **54**, 11169 (1996).

[33] P. E. Blöchl, Projector augmented-wave method, Phys. Rev. B **50**, 17953 (1994).

[34] G. Kresse and D. Joubert, From ultrasoft pseudopotentials to the projector augmented-wave method, Phys. Rev. B **59**, 1758 (1999).

[35] J. P. Perdew, K. Burke, and M. Ernzerhof, Generalized gradient approximation made simple, Phys. Rev. Lett. **77**, 3865 (1996).

[36] S. Grimme, J. Antony, S. Ehrlich, and H. Krieg, A consistent and accurate *ab initio* parametrization of density functional dispersion correction (DFT-D) for the 94 elements H-Pu, J. Chem. Phys. **132**, 154104 (2010).

[37] S. Grimme, S. Ehrlich, and L. Goerigk, Effect of the damping function in dispersion corrected density functional theory, J. Comput. Chem. **32**, 1456 (2011).

[38] L. Liang and V. Meunier, Electronic structure of assembled graphene nanoribbons: Substrate and many-body effects, Phys. Rev. B **86**, 195404 (2012).

[39] A. Basagni, F. Sedona, C. A. Pignedoli, M. Cattelan, L. Nicolas, M. Casarin, and M. Sambi, Molecules-oligomers-nanowires-graphene nanoribbons: A bottom-up stepwise on-surface covalent synthesis preserving long-range order, J. Am. Chem. Soc. **137**, 1802 (2015).

[40] M. Yano, S. Yasuda, K. Fukutani, and H. Asaoka, Long and oriented graphene nanoribbon synthesis from well-ordered 10,10'-dibromo-9,9'-bianthracene monolayer on crystalline au surfaces, RSC Adv. **13**, 14089 (2023).

[41] G. Langewisch, J. Falter, H. Fuchs, and A. Schirmeisen, Forces during the controlled displacement of organic molecules, Phys. Rev. Lett. **110**, 036101 (2013).

[42] D. Lock, S. Sakulsermsuk, R. E. Palmer, and P. A. Sloan, Mapping the site-specific potential energy landscape for chemisorbed and physisorbed aromatic molecules on the Si(111)-7 × 7 surface by time-lapse STM, J. Phys.: Condens. Matter **27**, 054003 (2015).

[43] B. Such, T. Trevethan, T. Glatzel, S. Kawai, L. Zimmerli, E. Meyer, A. L. Shluger, C. H. M. Amijs, P. de Mendoza, and A. M. Echavarren, Functionalized truxenes: Adsorption and diffusion of single molecules on the KBr(001) surface, ACS Nano **4**, 3429 (2010).

[44] J. Gehrig, M. Penedo, M. Parschau, J. Schwenk, M. A. Marioni, E. W. Hudson, and H. J. Hug, Surface single-molecule dynamics controlled by entropy at low temperatures, Nat. Commun. **8**, 14404 (2017).

[45] F. Hanke and J. Björk, Structure and local reactivity of the Au(111) surface reconstruction, Phys. Rev. B **87**, 235422 (2013).

[46] L. Gigli, N. Manini, A. Benassi, E. Tosatti, A. Vanossi, and R. Guerra, Graphene nanoribbons on gold: Understanding superlubricity and edge effects, 2D Mater. **4**, 045003 (2017).

[47] J. Eifler, POSCAR Structures of different orientaton of GNR on Au(111), Zenodo (2025), https://doi.org/10.5281/zenodo.17549356.

[48] G. Kresse and J. Hafner, *Ab initio* molecular dynamics for liquid metals, Phys. Rev. B **47**, 558 (1993).

[49] G. Henkelman, B. P. Uberuaga, and H. Jónsson, A climbing image nudged elastic band method for finding saddle points and minimum energy paths, J. Chem. Phys. **113**, 9901 (2000).

[50] E. Bitzek, P. Koskinen, F. Gähler, M. Moseler, and P. Gumbsch, Structural relaxation made simple, Phys. Rev. Lett. **97**, 170201 (2006).